# Automated Electrodes Detection during simultaneous EEG/fMRI

Mathis Fleury[*], Christian Barillot [*], Marsel Mano [*], Elise Bannier [†], Pierre Maurel [*]

2018
March

## 1 Abstract

The coupling of EEG/fMRI allows measuring brain activity at high spatio-temporal resolution. The localisation of EEG sources depends on several parameters including the position of the electrodes on the scalp. An accurate knowledge about this information is important for source reconstruction. Currently, when acquiring EEG/fMRI together, the position of the electrodes is generally estimated according to fiducial points by using a template. In the context of simultaneous EEG/fMRI acquisition, a natural idea is to use MR images to localise EEG electrodes. However, MR compatible electrodes are built to be almost invisible on MR Images. Taking advantage of a recently proposed Ultra-Short Echo Time (UTE) sequence, we introduce a fully automatic method to detect and label those electrodes in MR images. Our method was tested on 8 subjects wearing a 64-channel EEG cap. This automated method showed an average detection accuracy of 94% and the average position error was 3.1 mm. These results suggest that the proposed method has potential for determining the position of the electrodes during simultaneous EEG/fMRI acquisition.

## 2 Introduction

Electroencephalography (EEG) measures the electrical potential generated by the neuronal activity over the scalp with electrodes placed on the surface of the scalp ([Buzsáki et al., 2012]; [Murakami and Okada, 2006] [Petsche et al., 1984]). Usually electrodes are placed thanks to a flexible cap and positioned according to anatomical points enabling optimal covering of brain regions regardless of the size and shape of the subject's head. Currently, when acquiring EEG/fMRI simultaneously, the position of the electrodes is calculated according to fiducial points (anatomical points of the skull) such as Inion, Nasion and Vertex ([Strobel et al., 2008]). The localisation of EEG sources in the brain depends on several parameters including the position of the electrodes on the scalp. A precise knowledge of these positions is important because inaccurate information on EEG electrodes coordinates may affect EEG inverse solution ([Khosla et al., 1999]). In the context of simultaneous acquisition of EEG and MRI, this localisation is

[*]Univ Rennes, Inria, CNRS, Inserm, IRISA UMR 6074, VISAGES ERL U-1228, F-35000, Rennes
[†]Univ Rennes, Inria, CNRS, Inserm, IRISA UMR 6074, VISAGES ERL U-1228, F-35000, Rennes, University Hospital of Rennnes Department Radiology, Rennes, France

even more crucial/important. As a matter of fact, MRI and EEG need to be registered, for example, to be able to compare activation given by fMRI and by EEG. Other methods of electrodes localisation exist but require additional hardware like ([Koessler et al., 2011]) and can be uncomfortable for the subject if he must stay still during acquisition ([Le et al., 1998]).

Recently, a MRI sequence with radial k-space sampling named UTE for Ultra-short Echo-Time has been developed. It allows to visualise the tissues with a very short T2 and T2 *, such as cortical bone, tendons, ligaments ([Holmes and Bydder, 2005], [Keereman et al., 2010]). This sequence is all the more interesting in that it enables the visualisation of the MR compatible electrodes ([Butler et al., 2017], [Springer et al., 2008]) on the scalp.

We propose a fully automated method, which provides reliable and reproducible results for the detection and labelling of a MR compatible EEG cap into the MR space.

# 3 Methods

The retrieval of the electrodes consisted in two parts; firstly, we provided a mask that include the volume where the electrodes are located; secondly, we performed the electrode detection inside this volume of interest (VOI) (cf. Figure1). We hypothesised that electrodes will appear as spheres inside the UTE volume and it allows us to perform a Hough transform in a consistent manner across subjects.

## 3.1 Scalp segmentation

Because the UTE sequence is very noisy and also not very common in neuroimaging studies, it is more reliable to use the T1-w for the segmentation, the T1-w is registered on the UTE. The anatomical T1 image is then segmented using FSL, an open-library of analysis tools for MRI and its function BET (Brain Extraction Tool) ([Smith, 2002]; [Popescu et al., 2012]), a mask of the scalp is computed from the segmentation. Since electrodes are located around the head of the subject, the scalp mask is dilated in order to isolate this layer (cf. figure 1). What is outside the dilated mask is subtracted in order to isolate only the layer where the electrodes are located.

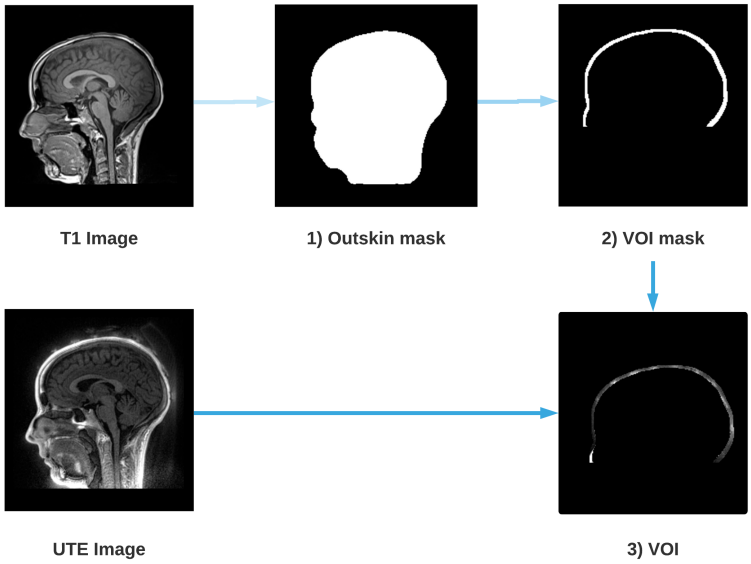


Figure 1: Steps for the extraction of the Volume Of Interest (VOI). An outskin mask is performed from the T1 image (1), then a dilation and a removal of the mask is performed (2) in order to obtain the layer where the electrodes are located. Finally, an operation of masking between the UTE image and the VOI gives us the VOI (3).

## 3.2 Detection of electrodes with the Spherical Hough transform

A 3D Hough transform was used to segment the electrodes inside the VOI. Hough transform is typically used to detect circle in 2D image, but was recently extended to detect 3D spheres ([Xie et al., 2012]). As the shape of an electrode can be assimilated to a sphere, the Spherical Hough Transformation algorithm seemed particularly well adapted to this task. The VOI image is first smoothed using a Gaussian kernel, with a FWHM adapted to the size of the electrode in order to reduce the noise of the image while saving electrode information. Then, the Hough algorithm is performed and provides a list of $n$ potential electrodes $[d_1...d_n] \in D$ (cf. Figure 2). Because the VOI includes also anatomical structures (nose, ears) and noise (artefacts due to the cap or gel), the number of potentially detected electrodes is substantially higher than the number of "true" electrodes $N$, in our case 64.

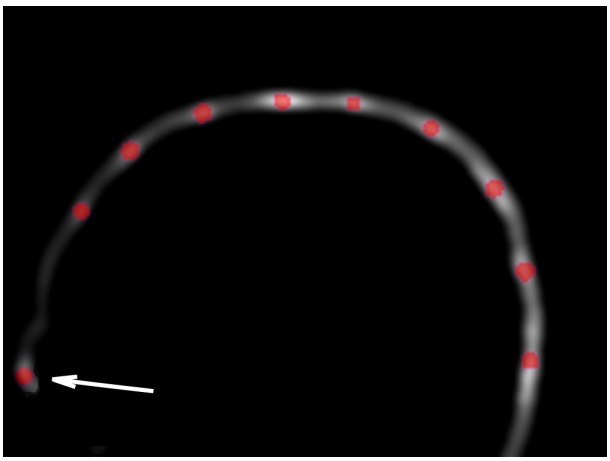

Figure 2: Example of Hough transform detection (red dots) on the VOI smoothed image. Hough transform detects also anatomical parts (arrow), which will be excluded in the filtering steps (cf. section 3.3).

### 3.3 Selection of detected electrodes

The detected electrodes are then filtered to keep only the "true" electrodes based on the distance between the detected and the actual position. A 64 electrodes spherical EEG template $p_j$ $(1 \leq j \leq 64)$ $\in P$ was used in conjunction with a Iterative Closest Point (ICP) algorithm to register the template onto the detected electrodes. The ICP will find the optimal rotation, translation and scale to fit the data point set D obtained with the Hough transform and the model point P. The algorithm is divided into 2 steps; a first step consists in assigning to a set $C$ of pairs of points, the detected points $D$ to the points of the model $P$. The second step consists of calculating the displacement that best aligns the matched points and applying this transformation to the points of the model.

The first step of the ICP algorithm will be to construct the set of matched points C. For each point in set D, the point of the nearest P model is found from the nearest neighbour. The set of paired points is formed based on the Euclidean distance between the points $d_i$ and $p_j$:

$$c_j = \arg\min_{d_i} \mathrm{dist}(d_i, p_j). \tag{1}$$

The second step consisted in computing the similarity transform that best aligns $c_j$ to $p_j$. The minimisation is expressed by:

$$(R^*, S^*, t^*) = \arg\min_{R,S,t} \sum_{j \in C} \|c_j - SRp_j - t\|^2, \tag{2}$$

where R is a rotation matrix (3 x 3), t is a translation vector (3 x 1) and S is a scale matrix ($S = s * Id$, 3 x 3). The ICP runs until convergence. The registered template $P^{'}$ can be written as:

$$p_j^{'} = RSp_j + t. \tag{3}$$

Once the ICP is complete, a two-part filtering phase is implemented. The first part consists in taking the closest point of the Hough transform data set; for each of the 64 electrodes of the registered model $P'$, the closest detected point $c_j$ is selected (see Figure 4). Unselected points are discarded.

Once the first filtering step is performed, the number of electrodes is equal to the total number of electrodes desired (64 in our case).

For the second part, all points $c_j$, which are farther away than 4 times the Median Absolute Deviation (MAD) to the closest point of the template $P^{'}$, are removed. For each removed point, a replacement is determined by a new detection from the local maxima on the VOI image around the theoretical position given by the registered template (cf. Figure 3). The new data set $D'$ is obtained and the 64 electrodes are then labelled again using the template.

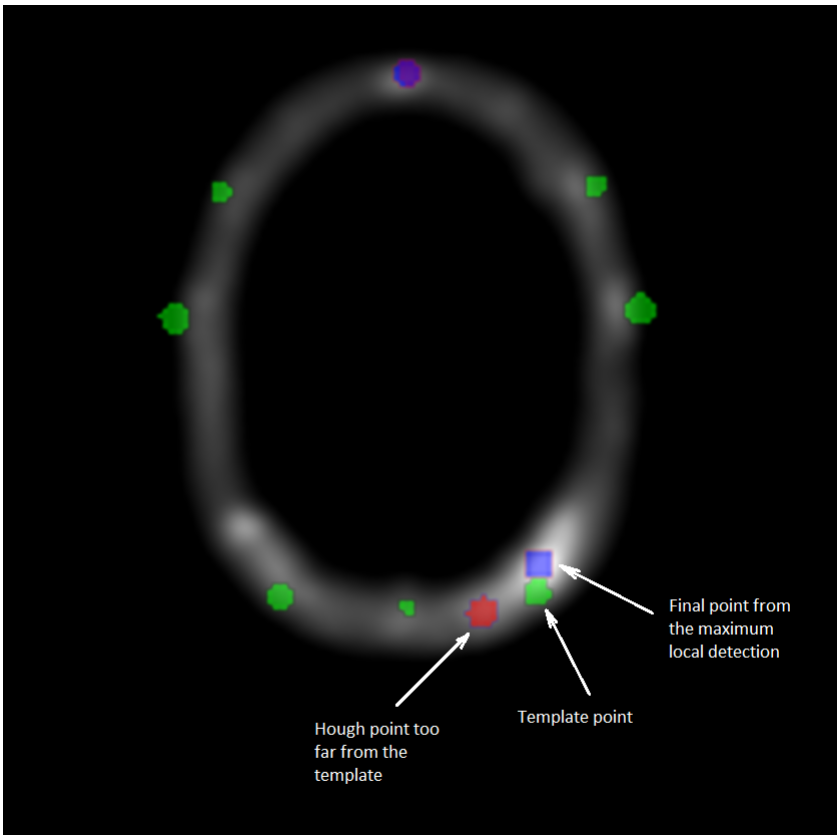


Figure 3: Cross section of the VOI image. Green points are corresponding to the template data set, blue points to the maximum local detection and the red one are the outliers. Replacing a point from the Hough data set too far from the registered template P'. The replaced point comes from a detection by local maxima closest to the template P'.

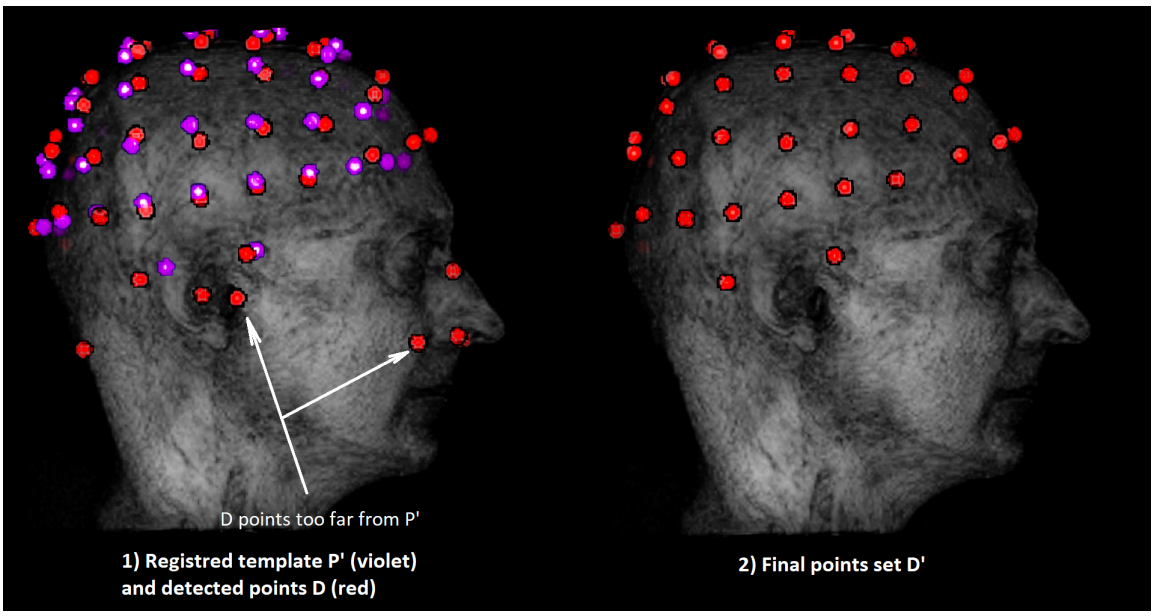


Figure 4: Example of outliers removal in potential electrodes data set $D$ with the ICP algorithm. The dataset $D$ is represented on the left and the final data set $D'$ with the filtering step on the right. Outliers are mostly due to external anatomical parts or noise not taken in account during the segmentation.

### 3.4 Validation of the method

A manual selection of the electrodes positions was done on the UTE sequence and the quality of our detection was assessed using this manual selection as a ground truth. Instead of selecting the centre of each electrodes in a 3D image, we choose to use a more convenient procedure for the manual detection. Following [Butler et al., 2017], the manual detection was performed by picking up the Cartesian position (x,y,z) of each 64 electrodes for each subject on a pancake view, which is roughly a 2D projection of the scalp ([de Munck et al., 2012]).

The performance indicators of our automated detection will be position error (PE) and positive predictive value (PPV). The position error is the average Euclidean distance between each pair of electrodes and the PPV is the percentage of electrodes that have been well detected (i.e. detected electrodes whose distance from the manually selected ones is below 10 mm which is the radius of the electrode).

## 4 Materials

### 4.1 Subjects and EEG equipment

The UTE sequence was acquired in height healthy volunteers and all underwent a simultaneous EEG/fMRI examination. A 64-channels MR compatible cap (Brainproduct, Gilching, Germany) was used for all the subjects and a particular attention has been given to its positioning according to standard fiducial points.

### 4.2 UTE sequences parameters

All MR data were collected with a 3T Siemens Verio MR scanner. Specifically, the UTE sequence using 3D radial k-space sampling was performed with the following parameters: repetition time (TR) = 3.45 ms, echo time (TE) = 0.07 ms, flip angle = 14° and voxel size ≈ 1.33x1.33x1.33 $mm^3$. A 3D T1 MPRAGE was also performed: TR = 1900ms, TE = 2.26, FA = 9° and voxel size ≈ 1.00x1.00x1.00 $mm^3$ . Two additional UTE sequences with different sampling have been acquired in order to decrease the acquisition time and to visualise the impact on electrodes detection. To reduce the acquisition time, the number of spokes has to decrease; from 60000 spokes (60K) for the original, 30000 (30K) and 15000 (15K) spokes for the additional. The UTE acquisition time goes down from 5min35s to 2min47 and 1min23s (cf. Figure 5).

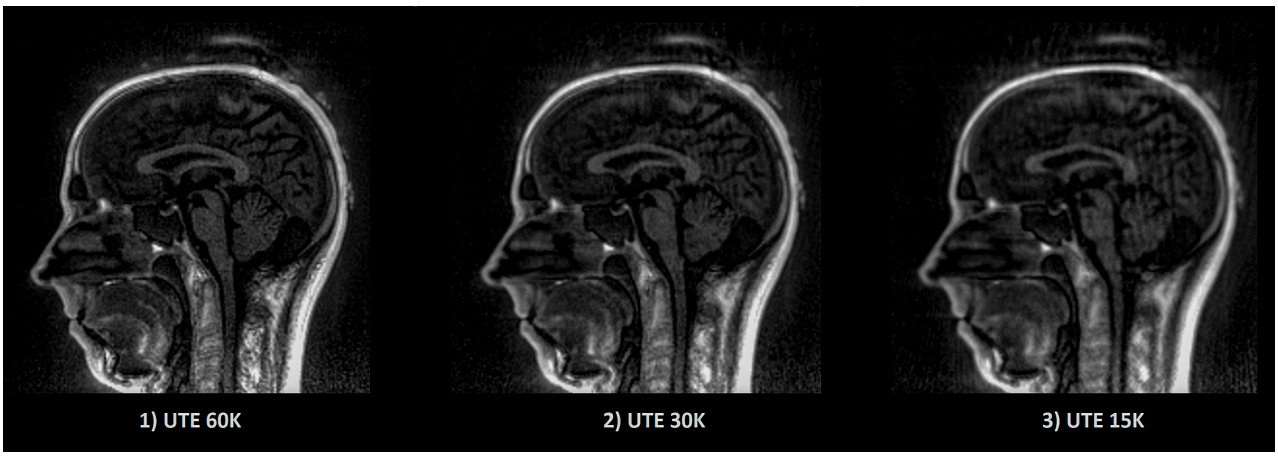


Figure 5: Example of UTE images with different sampling. The image quality as well as the acquisition time decrease linearly according to the sampling. Acquisition time for 1) 5.35min, 2) 2.47min, 3) 1.23min.

## 5 Results

The creation of an image (VOI) containing only the information related to the electrode allow to remove external noise while protecting the information related to the electrode. This image enables robust detection of the position of the electrodes for all subjects. Knowing that the number of electrodes detected is never superior to 64, the number of false positives and false negatives is mingled, indeed, a false positive corresponds to an electrode presented as detected but too far from the manual detection, and a false negative corresponds to an electrode which has not been detected. In our case, the number of false negatives and false positives is the same since 64 electrodes are detected each time. This number, however, does not exceed on average more than 6% of the total number of electrodes illustrates by the table 1. The detection accuracy represented by the positive predictive value (PPV) correspond to the percentage of electrodes correctly found. Our UTE-based electrode detection showed an average position error (PE) of 3.1mm for all subjects.

| | Subjects | Mean PE (mm) | Std PE (mm) | Max PE (mm) | PPV (%) |
|---|---|---|---|---|---|
| UTE | S1 | 2.73 | 2.83 | 17.32 | 95.38 |
| | S2 | 2.41 | 2.38 | 12.43 | 96.92 |
| | S3 | 2.66 | 2.43 | 13.62 | 95.38 |
| | S4 | 4.10 | 3.97 | 21.3 | 89.23 |
| | S5 | 3.32 | 3.38 | 14.45 | 90.7 |
| | S6 | 2.85 | 3.24 | 17.57 | 95.38 |
| | S7 | 2.76 | 2.51 | 15.90 | 96.92 |
| | S8 | 3.69 | 5.13 | 26.24 | 93.84 |
| FID | S1 | 7.60 | 3.09 | 15.31 | 76.92 |
| | S2 | 7.79 | 2.85 | 14.63 | 72.30 |
| | S3 | 6.15 | 2.71 | 13.45 | 90.76 |
| | S4 | 7.70 | 3.41 | 17.78 | 73.84 |
| | S5 | 6.08 | 2.78 | 16.36 | 90.76 |
| | S6 | 6.54 | 3.40 | 17.47 | 87.69 |
| | S7 | 6.88 | 3.39 | 17.10 | 87.69 |
| | S8 | 12.55 | 6.36 | 30.6 | 55.38 |

Table 1: Positive predictive value (PPV) and position error (PE) for each subject (S1-S8) for UTE-MR electrodes detection. The PPV is the percentage of electrodes that have been detected. We consider that an electrode is well localised when the PE is below 10mm ([Kavanagk et al., 1978]).

We then compared the performance of our method against a more classical semi-automatic one: five fiducial points were obtained manually and the spherical template was adjusted to these points [Towle et al., 1993]. The PE and PPV were also calculated in the same way as our method (cf figure 6). Paired t-test channel-by-channel of PEs were computed between the two groups and a significant difference was obtained ($p<0.0001$). The max PE reflected a high difficulty to detect the electrodes near anatomical parts or in posterior regions where the head apply a pressure.

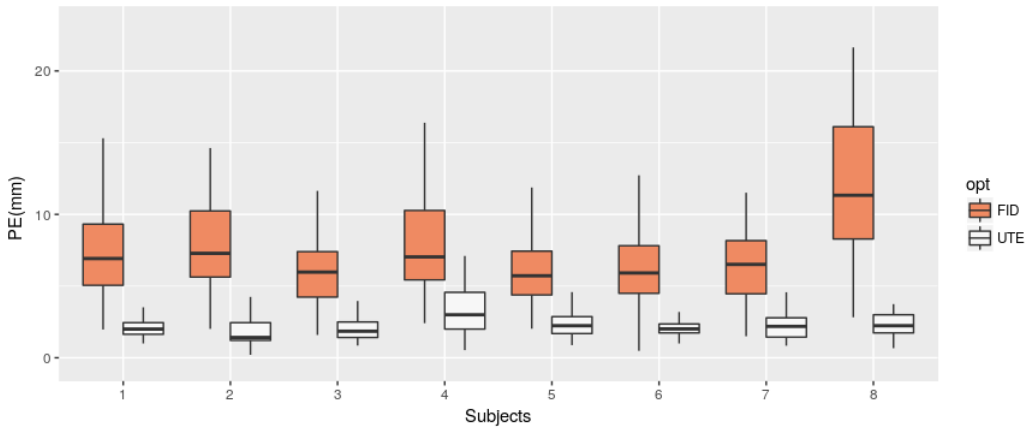


Figure 6: Position Error (PE) for UTE-based electrodes detection method and the semi-automatic method based on fiducial points (FID). Box-plots for the eight subjects are showed.

We also determine the impact of electrode detection on lower sample UTE sequences allowing to reduce the acquisition time, we tested two others UTE sequence (cf. Section 4.2). The sampling reduction of the UTE sequence has the effect of reducing the amount of information and decreasing the signal-to-noise ratio (cf. Figure 5) . This has a direct impact on the image quality and also on the electrodes detection.

We compared the three different images (cf. Figure 2) with the same detection system and the same parameters as the original UTE (60K). The mislocalisation as well as the position error increase according to the decrease of the sampling.

| | UTE 60K | UTE 30K | UTE 15K |
|---|---|---|---|
| PE (mm) | 3.12 | 4.02 | 6.56 |
| PPV (%) | 94.22 | 88.13 | 80.43 |

Table 2: The mean positive predictive value (PPV) and the mean of position error (PE) for Subjects 2 to 8, the subject 1 did not receive the additional sequences. The sampling decline decreases the detection accuracy and increases the position error.

# 6 Discussion

We have proposed an automated method for detecting and labelling EEG electrodes based on UTE MR images without using any external sensors. Previous results indicate that a localisation technique using electromagnetic digitisation technology is time-consuming [Dalal et al., 2014] and others techniques such as 3D digitisation can be affected by errors of registration and projection of EEG electrodes on the head model. We have shown that our method offers constant and precise results. Moreover, the proposed method provides the position of the electrodes directly into the MR-space.

The method presented here requires an additional sequence (the UTE acquisition sequence) in the experimental protocol. This acquisition takes roughly from 1 to 5 min. From our experiments, a

good compromise between acquisition time and detection quality can be achieved with a 2 or 3 min sequence. Optimisation of the sequence parameters could enable an improvement of the images without increasing the acquisition time.

# 7 Conclusion

We present a method to automatically detect and label EEG electrodes (64-channels) during an EEG/fMRI acquisition. We use a UTE MR sequence to obtain electrodes positions on a MR-volume. This method only has for additional cost the acquisition time of the UTE sequence in the MR protocol. We have demonstrated that our method has a significantly more accurate electrode detection compared to a semi-automatic detection method that is more commonly used during EEG/fMRI protocols. For future research, since the proposed method can be totally automated and does not require complex processing, this technique may be used to extract the position and the label of the electrodes in real time. Indeed, this technique is interesting for applications requiring immediate knowledge of the position of the electrodes. We believe this method will be useful in the improvement of the fusion of EEG-fMRI signals.

# References

[Butler et al., 2017] Butler, R., Gilbert, G., Descoteaux, M., Bernier, P.-M., and Whittingstall, K. (2017). Application of polymer sensitive MRI sequence to localization of EEG electrodes.

[Buzsáki et al., 2012] Buzsáki, G., Anastassiou, C. A., and Koch, C. (2012). The origin of extracellular fields and currents — EEG, ECoG, LFP and spikes. *Nature Reviews Neuroscience*, 13(6):407–420.

[Dalal et al., 2014] Dalal, S. S., Rampp, S., Willomitzer, F., and Ettl, S. (2014). Consequences of EEG electrode position error on ultimate beamformer source reconstruction performance. *Frontiers in Neuroscience*, 8:42.

[de Munck et al., 2012] de Munck, J. C., van Houdt, P. J., Verdaasdonk, R. M., and Ossenblok, P. P. (2012). A semi-automatic method to determine electrode positions and labels from gel artifacts in EEG/fMRI-studies. *NeuroImage*, 59(1):399–403.

[Holmes and Bydder, 2005] Holmes, J. E. and Bydder, G. M. (2005). MR imaging with ultrashort TE (UTE) pulse sequences: Basic principles. *Radiography*, 11(3):163–174.

[Kavanagk et al., 1978] Kavanagk, R. N., Darcey, T. M., Lehmann, D., and Fender, D. H. (1978). Evaluation of methods for three-dimensional localization of electrical sources in the human brain. *IEEE Transactions on Biomedical Engineering*, (5):421–429.

[Keereman et al., 2010] Keereman, V., Fierens, Y., Broux, T., De Deene, Y., Lonneux, M., and Vandenberghe, S. (2010). Mri-based attenuation correction for pet/mri using ultrashort echo time sequences. *Journal of nuclear medicine*, 51(5):812–818.

[Khosla et al., 1999] Khosla, D., Don, M., and Kwong, B. (1999). Spatial mislocalization of eeg electrodes–effects on accuracy of dipole estimation. *Clinical neurophysiology*, 110(2):261–271.

[Koessler et al., 2011] Koessler, L., Cecchin, T., Caspary, O., Benhadid, A., Vespignani, H., and Maillard, L. (2011). EEG–MRI Co-registration and Sensor Labeling Using a 3D Laser Scanner. *Annals of Biomedical Engineering*, 39(3):983–995.

[Le et al., 1998] Le, J., Lu, M., Pellouchoud, E., and Gevins, A. (1998). A rapid method for determining standard 10/10 electrode positions for high resolution eeg studies. *Electroencephalography and clinical neurophysiology*, 106(6):554–558.

[Murakami and Okada, 2006] Murakami, S. and Okada, Y. (2006). Contributions of principal neocortical neurons to magnetoencephalography and electroencephalography signals. *The Journal of physiology*, 575(3):925–936.

[Petsche et al., 1984] Petsche, H., Pockberger, H., and Rappelsberger, P. (1984). On the search for the sources of the electroencephalogram. *Neuroscience*, 11(1):1–27.

[Popescu et al., 2012] Popescu, V., Battaglini, M., Hoogstrate, W., Verfaillie, S., Sluimer, I., van Schijndel, R., van Dijk, B., Cover, K., Knol, D., Jenkinson, M., Barkhof, F., de Stefano, N., and Vrenken, H. (2012). Optimizing parameter choice for FSL-Brain Extraction Tool (BET) on 3D T1 images in multiple sclerosis. *NeuroImage*, 61(4):1484–1494.

[Smith, 2002] Smith, S. M. (2002). Fast robust automated brain extraction. *Human Brain Mapping*, 17(3):143–155.

[Springer et al., 2008] Springer, F., Martirosian, P., Schwenzer, N. F., Szimtenings, M., Kreisler, P., Claussen, C. D., and Schick, F. (2008). Three-dimensional ultrashort echo time imaging of solid polymers on a 3-tesla whole-body mri scanner. *Investigative radiology*, 43(11):802–808.

[Strobel et al., 2008] Strobel, A., Debener, S., Sorger, B., Peters, J. C., Kranczioch, C., Hoechstetter, K., Engel, A. K., Brocke, B., and Goebel, R. (2008). Novelty and target processing during an auditory novelty oddball: A simultaneous event-related potential and functional magnetic resonance imaging study. *NeuroImage*, 40(2):869–883.

[Towle et al., 1993] Towle, V. L., Bolaños, J., Suarez, D., Tan, K., Grzeszczuk, R., Levin, D. N., Cakmur, R., Frank, S. A., and Spire, J.-P. (1993). The spatial location of EEG electrodes: locating the best-fitting sphere relative to cortical anatomy. *Electroencephalography and Clinical Neurophysiology*, 86(1):1–6.

[Xie et al., 2012] Xie, L., Cianciolo, R. E., Hulette, B., Lee, H. W., Qi, Y., Cofer, G., and Johnson, G. A. (2012). Magnetic resonance histology of age-related nephropathy in the Sprague Dawley rat. *Toxicologic pathology*, 40(5):764–78.